DNS OF SWIRLING FLOW IN A ROTATING PIPE

Bikash Sahoo
Department of Mathematics
National Institute of Technology, Rourkela
Odisha, INDIA
bikashsahoo@nitrkl.ac.in

Frode Nygård
Statoil
Laberget 114, 4020 Stavanger, NORWAY
fron@statoil.com

Helge I. Andersson
Department of Energy and Process Engineering
Norwegian University of Science and Technology
Trondheim, NORWAY
helge.i.andersson@ntnu.no

ABSTRACT

Numerical simulation is carried out to study the combined effects of rotation and induced swirl on the fully developed turbulent pipe flow at Reynolds number $Re_b = 4900$, based on the bulk velocity and the pipe diameter. The swirl is induced by a body force in the tangential momentum equation, which produces a tangential velocity field in the near wall region. Results from a single swirl along with five different strengths of the rotation are considered. The effects of rotation and swirl on turbulent structures are investigated in detail. Also instantaneous axial velocity fluctuations are provided to visualize the effects on the turbulent structures.

Introduction

Turbulent flows of liquids or gases through long straight pipes occur in a variety of different industrial applications. Such flows have received considerable attention throughout the years and are fairly well understood today, although some uncertainties still prevails at very high Reynolds numbers; see e.g. Hultmark *et al.* (2012). Under certain circumstances, however, the streamlines are helical rather than straight lines and the mean flow becomes two-componential rather than one-componential. This happens if a swirling motion arises or if the pipe is subjected to axial rotation. Swirl may result from a swirl generator or an upstream elbow, whereas axially rotating pipes are found in turbo machinery cooling systems. In both cases, a circumferential component U_θ of the mean velocity vector coexists with the axial mean velocity component U_z. The presence of a circumferential mean velocity component tends to orient the coherent near-wall structures with the local mean flow direction. Besides the tilting of the near-wall structures, the structures may be strengthened or weakened in a two-componential mean flow.

Fully developed turbulent flow in axially rotating pipes has been studied experimentally by Murakami & Kikuyama (1980) and Imao *et al.* (1996) and by means of large-eddy simulations (LES) by Eggels & Nieuwstadt (1993) and direct numerical simulations (DNS) by Eggels *et al.* (1994) and Orlandi & Fatica (1997). It is observed that rotation results in drag reduction. Recent DNS studies of swirling pipe flow by Nygard & Andersson (2010) showed the same influence of the induced swirl on the axial mean velocity as axial rotation. However, the presence of swirl turned out to have less clear-cut effects on the turbulence field. In the cases with stronger swirl, even drag reduction was reported whereas weak swirl gave rise to excess drag.

Swirl and axial rotation both give rise to helical streamlines and it is therefore not unexpected that similarities between these two circumstances can be found. The aim of the present study is to examine how an originally swirling pipe flow reacts to axial rotation. For a given swirl number, five different rotation rates ($N = -1, -0.5, 0, 0.5, 1$) with both senses of rotation will be studied. To this end, the full Navier-Stokes equations are solved in three-dimensional space and in time on a computational mesh sufficiently fine to resolve the energetic large-eddy structures.

Governing equations

The governing equations are solved in cylindrical coordinates θ, r, and z. For practical reasons, the variables $q_\theta = ru_\theta$, $q_r = ru_r$ and $q_z = u_z$ are introduced. Here u_θ, u_r, and u_z are velocity components in the respective coordinate directions. All variables in the governing equations are non-dimensionalized with the centerline velocity of the Poiseuille profile, U_p and the pipe radius, R.

To simplify, the non-dimensionalized total pressure, p_{total} is divided in to three parts as follows:

$$p_{\text{total}} = \hat{P}(\theta) + \bar{P}(z) + p(\theta, r, z, t). \qquad (1)$$

The first part, $\hat{P}(\theta)$, is the artificial transverse pressure component. In order to introduce a swirl in the pipe flow, the azimuthal pressure gradient, $d\hat{P}/d\theta$, is introduced. The second part of Eq. (1) is the mean axial pressure, $\bar{P}(z)$ and finally, $p(\theta, r, z, t)$ represents the remaining part of the total pressure. The Navier-Stokes equations in terms of the new variables, in a reference frame rotating with the pipe wall around the z-axis are

$$\frac{\partial q_\theta}{\partial t}+\frac{\partial q_\theta/r q_r}{\partial r}+\frac{1}{r^2}\frac{\partial q_\theta^2}{\partial \theta}+\frac{\partial q_\theta q_z}{\partial z}+\frac{q_\theta}{r}\frac{q_r}{r}+Nq_r$$
$$=-\frac{\partial p}{\partial \theta}-\frac{d\hat{P}}{d\theta}+\frac{1}{Re_b}\Big[\frac{\partial}{\partial r}r\frac{\partial q_\theta/r}{\partial r}-\frac{q_\theta}{r^2}+\frac{1}{r^2}\frac{\partial^2 q_\theta}{\partial \theta^2}$$
$$+\frac{\partial^2 q_\theta}{\partial z^2}+\frac{2}{r^2}\frac{\partial q_r}{\partial \theta}\Big] \tag{2}$$

$$\frac{\partial q_r}{\partial t}+\frac{\partial}{\partial r}\frac{q_r^2}{r}+\frac{\partial}{\partial \theta}\frac{q_\theta q_r}{r^2}+\frac{\partial q_r q_z}{\partial z}-\frac{q_\theta^2}{r^2}-Nq_\theta$$
$$=-r\frac{\partial p}{\partial r}+\frac{1}{Re_b}\Big[\frac{\partial}{\partial r}r\frac{\partial q_r/r}{\partial r}-\frac{q_r}{r^2}+\frac{1}{r^2}\frac{\partial^2 q_r}{\partial \theta^2}+\frac{\partial^2 q_r}{\partial z^2}-\frac{2}{r^2}\frac{\partial q_\theta}{\partial \theta}\Big] \tag{3}$$

$$\frac{\partial q_z}{\partial t}+\frac{1}{r}\frac{\partial q_r q_z}{\partial r}+\frac{1}{r^2}\frac{\partial q_\theta q_z}{\partial \theta}+\frac{\partial q_z^2}{\partial z}=-\frac{\partial p}{\partial z}-\frac{d\overline{P}}{dz}$$
$$+\frac{1}{Re_b}\Big[\frac{1}{r}\frac{\partial}{\partial r}r\frac{\partial q_z}{\partial r}+\frac{1}{r^2}\frac{\partial^2 q_z}{\partial \theta^2}+\frac{\partial^2 q_z}{\partial z^2}\Big] \tag{4}$$

where $N = 2\Omega R/U_p$ is the non-dimensional rotational number.

The bulk Reynolds number Re_b is maintained at 4900 by enforcing a constant bulk velocity U_b in the axial direction, which in turn is sustained by the average pressure gradient $d\overline{P}/dz$, found in the axial momentum equation (4). The imposed non-dimensionalized azimuthal pressure gradient, $d\hat{P}/d\theta$ is designed to be constant and non-zero for $r > 0.9R$ and zero otherwise, as indicated by the shaded area in Fig. 1.

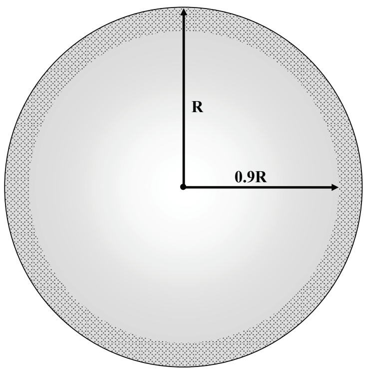

Figure 1. Cross-section of the circular pipe. The shaded annular region indicates the region where the azimuthal pressure gradient is imposed.

Numerical Method and Grid Configuration

The discretization of the momentum equations is generalized as in Orlandi & Fatica (1997) and Nygard & Andersson (2010)

$$(1-\alpha_l\Delta t A_{i\theta})(1-\alpha_l\Delta t A_{ir})(1-\alpha_l\Delta t A_{iz})\Delta\hat{q}_i$$
$$=\Delta t[\gamma_l H_i^n+\rho_l H_i^{n-1}-\alpha_l\Psi_i p^n]+\Delta t[2\alpha_l(A_{i\theta}+A_{ir}+A_{iz})q_i^n] \tag{5}$$

where $i = 1,2,3$ and represent the θ, r, and z directions. $\Delta\hat{q}_i = \hat{q}_i - q_i^n$ and $\hat{q}$ is an intermediate velocity field. q_i^n is the velocity field at the old time step, n. H_i contains the discretized convective terms. $\Psi_i p^n$ and $A_{i\theta}, A_{ir}, A_{iz}$ represent the discretized pressure gradients and the discretized second-order derivatives, respectively. α_l, γ_l and ρ_l are the coefficients from the time advancement scheme. The approximate factorization technique is adopted to reduce the term in front of $\Delta\hat{q}_i$ to tri-diagonal matrices. The discretizations are forward in time and central in space. Here $\hat{q}$ is non-divergence free and is found by the use of a third-order hybrid Runge-Kutta/Crank-Nicolson method. An explicit third-order low storage Runge-Kutta method is used for the nonlinear terms and the linear terms are solved by an implicit Crank-Nicolson scheme. The method is second-order and third-order accurate in time for nonlinear and linear terms, respectively.

The DNS code is based on staggered grid. Accordingly the computational domain splits up into cells with the velocities calculated at the cell faces and the pressure calculated at the cell centers. All the cells are enclosed by six sides (see Fig. 2) except for the cells adjacent to the centerline. The grid is described by $N1 \times N2 \times N3$ where $N1$, $N2$ and $N3$ represent the number of grid points in θ, r and z directions, respectively. The grid is uniform along the azimuthal and axial directions and is non-uniform along the radial direction. Since, the fine grid requires much larger CPU-time and storage requirements, the present DNS simulation with induced swirl and pipe rotation has been carried out for $65 \times 97 \times 65$ grid points with $L_z = 10D$.

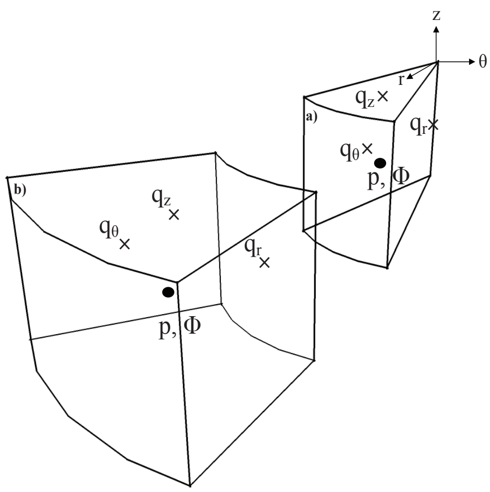

Figure 2. Computational cell: (a) next to the centerline and (b) all elsewhere.

1 Results and Discussions

Results from five cases with different values of rotation number N and swirl strength $d\hat{p}/d\theta = 0.0250$ are computed and are compared with the results from the DNS simulations by Nygard & Andersson (2008), without rotation, with $d\hat{p}/d\theta = 0.0250$ and grid size of $64 \times 96 \times 64$ (see Table 1). In Fig. 3, mean axial velocity profiles are plotted for the current simulations. The profile corresponding to $N = 0$ has evidently moved towards the laminar Poiseuille profile. Fig. 4 shows the simultaneous effects of swirl and rotation on the mean azimuthal velocity. It is clear that the amplitude of the normalized mean circumferential velocity is maximum for high value of opposite ($N = -1.0$) rotation.

Table 1. Simulation results with $N = 0$ and $\frac{d\hat{P}}{d\theta} = 0.0250$

	Present	Nygard & Andersson (2008)
$Re_c = U_c D/\nu$	7316	7320
$Re_\tau = u_\tau D/\nu$	324	327
U_c/u_τ	22.35	22.39
U_b/u_τ	14.95	14.98
U_c/U_b	1.45	1.49

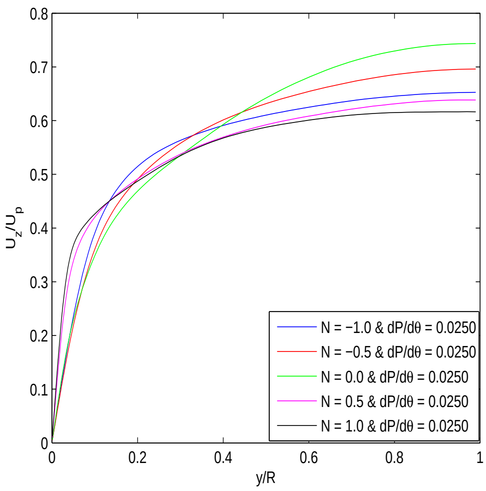

Figure 3. Mean axial velocity profiles.

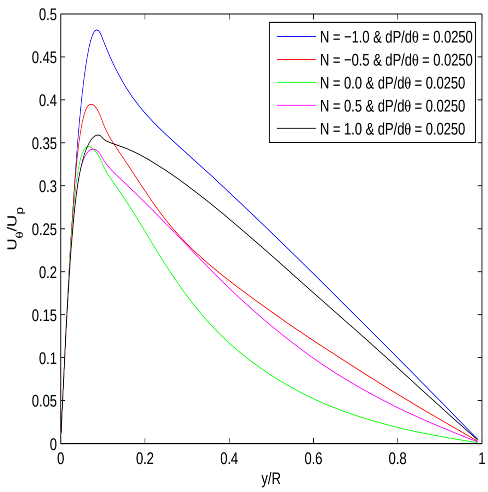

Figure 4. Mean circumferental velocity profiles.

Sweeps and ejections are the primary sources of the Reynolds shear stress $\langle u'_r u'_z \rangle$, shown in Fig. 5 and are responsible for the production of axial normal stress. The only non-negligible stress in a non-rotating pipe is $\langle u'_r u'_z \rangle$. When the pipe rotates, this stress is reduced and the other two stresses $\langle u'_r u'_\theta \rangle$ and $\langle u'_\theta u'_z \rangle$ increase. Fig. 5 shows the profile for $\langle u'_r u'_z \rangle$ attains highest peak corresponding to $N = 1$ and $d\hat{P}/d\theta = 0.0250$, and gets decreased as the rotation number tends to zero. The magnitude of the rz-component corresponding to the opposite ($N < 0$) rotation always remain less than that of corresponding to $N > 0$. This Reynolds shear stress component is a measure of the turbulent drag. It is evident that maximum drag reduction corresponds to $N = -0.5$ and $d\hat{P}/d\theta = 0.0250$. Fig. 6 shows in the core region of the flow, the behaviour of the flow of $\langle u'_r u'_\theta \rangle$ is almost linear. The $\langle u'_\theta u'_z \rangle$-profiles are shown in Fig. 7 and also here, pronounced effects in the near-wall region can be observed. The increase of the $\langle u'_r u'_\theta \rangle$ and $\langle u'_\theta u'_z \rangle$ components in the near-wall region is due to the large magnitude of the mean velocity gradient dU_θ/dr. Surprisingly, in presence of swirl, $\langle u'_\theta u'_z \rangle$ attains highest peak value for no-rotation ($N = 0$), as is clear from Fig. 7.

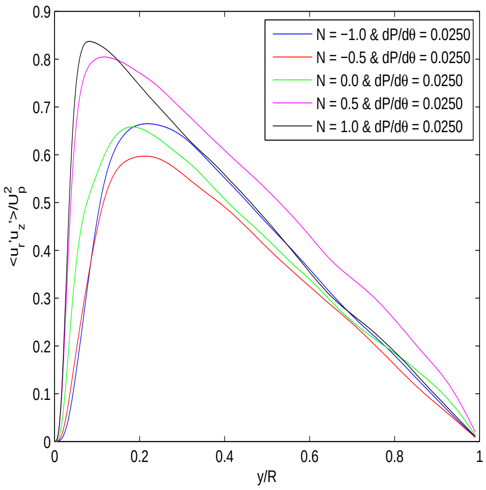

Figure 5. Reynolds shear stress profile for $\langle u'_r u'_z \rangle$-component.

Visualization

Controlling the coherent structures seems important in taming the turbulence. In accordance with this, visualization plots of instantaneous axial velocity fluctuations in $\theta - z$ plane are given in Figs. 8 to 12 for all the five cases, considered in this work. In these figures red and blue colors visualize positive and negative fluctuations respectively. It is clear that the presence of swirl creates a velocity field that tilts the streaks. On the other hand as the rotation number changes sign from negative to positive, the distance between the streaks increases. A reduction (increase) in the length of streaky structures due to negative (positive) fluctuations is observed as the rotation number, N changes sign from negative to positive (compare Figs. 9 and 11).

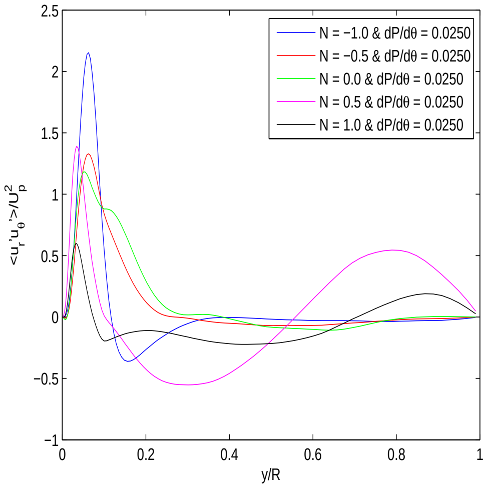

Figure 6. Reynolds shear stress profile for $\langle u_r' u_\theta' \rangle$-component.

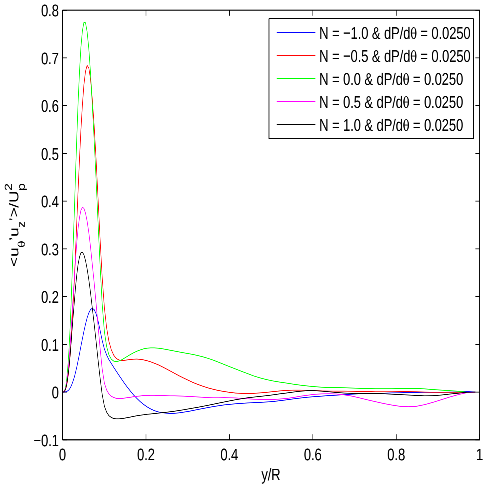

Figure 7. Reynolds shear stress profile for $\langle u_\theta' u_z' \rangle$-component.

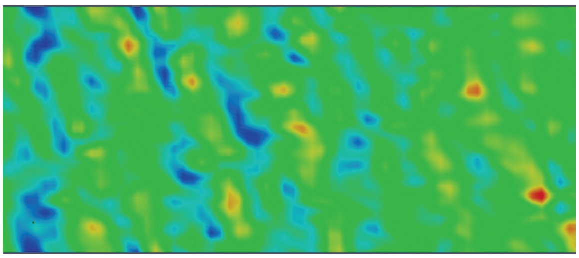

Figure 8. Visualisation of axial velocity fluctuations u_z'/U_p, at $y/R = 0.1$ for $N = -1.0$ and $d\hat{P}/d\theta = 0.0250$.

Conclusions

The work is devoted to the numerical simulation of a turbulent pipe flow with rotation and swirl induced by near-wall body force. The flow is three-dimensional. The numerical method is tested for the non-rotating case ($N = 0$) by comparing the results with Nygard & Andersson (2008). In presence of swirl, maximum drag reduction is achieved for $N = -0.5$. It has been taken in to consideration that

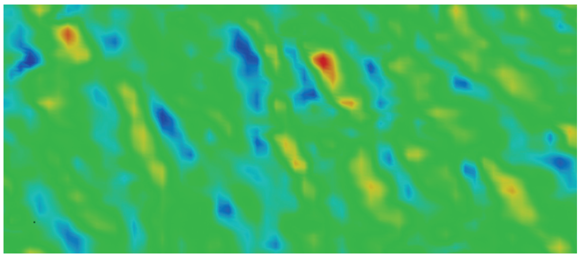

Figure 9. Visualisation of axial velocity fluctuations u_z'/U_p, at $y/R = 0.1$ for $N = -0.5$ and $d\hat{P}/d\theta = 0.0250$.

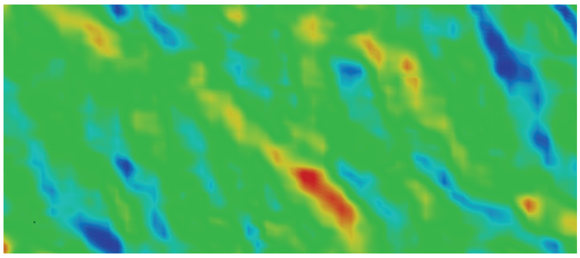

Figure 10. Visualisation of axial velocity fluctuations u_z'/U_p, at $y/R = 0.1$ for $N = 0$ and $d\hat{P}/d\theta = 0.0250$.

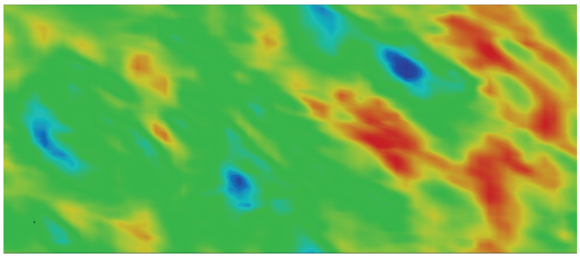

Figure 11. Visualisation of axial velocity fluctuations u_z'/U_p, at $y/R = 0.1$ for $N = 0.5$ and $d\hat{P}/d\theta = 0.0250$.

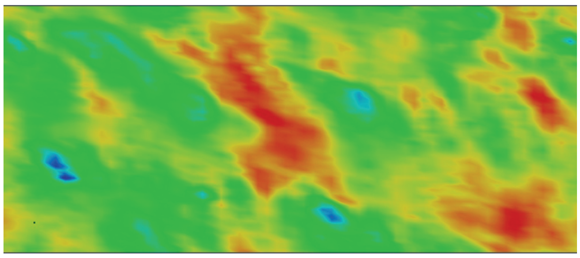

Figure 12. Visualisation of axial velocity fluctuations u_z'/U_p, at $y/R = 0.1$ for $N = 1.0$ and $d\hat{P}/d\theta = 0.0250$.

the simulation has been done with a relative coarse grid, which have an uncertain influence on the present results. Therefore, simulations with improved grid resolutions will be carried out in future work.

Acknowledgements

One of the authors (BS) is thankful to the Department of Science & Technology, Government of India for awarding the prestigious **BOYSCAST** Fellowship (SR/BY/M-

04/09) to pursue advanced research work at Norwegian University of Science and Technology (NTNU), Norway.

REFERENCES

Eggels, J.G.M. & Nieuwstadt, F.T.M. 1993 In *Proceedings of 9th Symposium on Turbulent Shear Flows*. Kyoto, Japan.

Eggels, J.G.M., Unger, F., Weiss, M.H., Westerweel, J., Adrian, R.J., Friedrich, R. & Nieuwstadt, F.T.M. 1994 Fully developed turbulent pipe flow: a comparison between direct numerical simulation and experiment. *J. Fluid Mech.* **268**, 175–209.

Hultmark, M., Vallikivi, M., Bailey, S.C.C. & Smits, A.J. 2012 Turbulent pipe flow at extreme Reynolds numbers. *Phys. Rev. Lett., 094501* **108**.

Imao, S., Itoh, M. & Harada, T. 1996 Turbulent characteristics of the flow in an axially rotating pipe. *Int. J. Heat Fluid Flow* **17**, 444–451.

Murakami, M. & Kikuyama, K. 1980 Turbulent flow in axially rotating pipes. *ASME J. Fluids Eng.* **102**, 97–103.

Nygard, F. & Andersson, H.I. 2008 Drag reduction in swirling pipe flow. In *Proceedings of 6th International Conference on CFD in Oil and Gas, Metallurgical and Process Industries*. SINTEF/NTNU, Trondheim, Norway.

Nygard, F. & Andersson, H.I. 2010 DNS of swirling turbulent pipe flow. *Int. Jr. Numer. Meth. Fluids* **64**, 945–972.

Orlandi, P. & Fatica, M. 1997 Direct simulation of turbulent flow in a pipe rotating about its axis. *J. Fluid Mech.* **343**, 43–72.